

**ASSESSMENT OF CFD CAPABILITY FOR
HYPERSONIC SHOCK WAVE LAMINAR BOUNDARY
LAYER INTERACTIONS USING PERFECT GAS
NAVIER-STOKES EQUATIONS**

BY

MEHRNAZ ROUHI YOUSSEFI

**A dissertation submitted to the
Graduate School—New Brunswick
Rutgers, The State University of New Jersey**

**In partial fulfillment of the requirements
For the degree of
Doctor of Philosophy**

Graduate Program in Mechanical and Aerospace Engineering

**Written under the direction of
Doyle D. Knight
And approved by**

New Brunswick, New Jersey

January, 2016

ABSTRACT OF THE DISSERTATION

Assessment of CFD Capability for Hypersonic Shock Wave Laminar Boundary Layer Interactions Using Perfect Gas Navier-Stokes Equations

by MEHRNAZ ROUHI YOUSSEFI

Dissertation Director:

Doyle D. Knight

The goal of this study is to assess CFD capability for prediction of laminar shock wave/boundary layer interactions at hypersonic velocities. More specifically, the flowfield over a double cone configuration is simulated using perfect gas assumptions and Navier-Stokes equations. Computations are compared with experimental data obtained from measurements conducted in the LEN5 XX shock tunnel at CUBRC. Four separate cases of freestream conditions are simulated to examine the numerical methods in a wide range of enthalpies. The results of this investigation can provide factors for design optimization of hypersonic air vehicles.

Table of Contents

Abstract	ii
List of Tables	v
List of Figures	vi
1. Introduction	1
1.1. Motivations	1
1.2. Review of Related Work	1
1.3. Scope of the Thesis	6
2. Description of Experiment	8
2.1. Introduction	8
2.2. LENS XX Facility	8
2.3. DoubleCone Experiments	10
3. Mathematical Formulation	12
3.1. Perfect Gas Laminar Navier-Stokes	12
3.1.1. Boundary Conditions	13
3.2. The Numerical Method	13
3.3. Grid Generation	13
3.4. Solution Schemes	15
3.4.1. Finite Volume Method	15
3.4.2. Van Leer's Method	18
3.4.3. Roe's Method with Harten Modification	19
3.5. The Limiter	21

3.6. Reconstruction	21
3.7. Temporal Quadrature	22
4. Results and Discussions	23
4.1. Results	23
4.1.1. Grid Refinement	25
4.2. Discussions	25
5. Conclusion	35

List of Tables

2.1. Freestream conditions for double cone experiments	11
3.1. Grid Sequences	14

List of Figures

2.1.	Representative $x - t$ diagram and schematic of LENS XX [19]	9
2.2.	Double cone configuration	10
4.1.	Computational results for Run 1, Table 2.1	26
4.2.	Flowfield structure for Run 1, Table 2.1	27
4.3.	Computational results for Run 2, Table 2.1	28
4.4.	Flowfield structure for Run 2, Table 2.1	29
4.5.	Computational results for Run 6, Table 2.1	30
4.6.	Flowfield structure for Run 6, Table 2.1	31
4.7.	Computational results for Run 4, Table 2.1	32
4.8.	Flowfield structure for Run 4, Table 2.1	33
4.9.	Computed results for Run 1, Table 2.1 for different grid refinement levels	34

Chapter 1

Introduction

1.1 Motivations

In modern aerodynamics, there are a large number of circumstances where shock waves are generated; when the flow passes a supersonic or hypersonic vehicle, shock waves are formed by either a change in the slope of a surface, a downstream obstacle or a back pressure constraining the flow to become subsonic. The interaction of a shock wave with a boundary layer results in complex phenomena because of the rapid retardation of the flow in the boundary layer, generation of separation bubbles, and the propagation of the shock in a multi layered structure. The consequences of shock wave/boundary layer interaction (SWBLI) are critical for the hypersonic vehicle performance. The adverse pressure gradients in the boundary layer and formation of the recirculation zones can result in adverse aerodynamic loading, drag rise, and high aerothermal heating. Hence, accurate modeling of the flowfield and heat transfer is crucial to overcome the aforementioned problems.

1.2 Review of Related Work

The problem of shock wave boundary layer interaction has received much attention [39, 32, 16, 17, 4, 23, 21, 15, 14]. In this introduction we first summarize the most important experimental studies conducted to date to measure the aerothermal loads generated in laminar hypersonic shock wave/ boundary layer interactions. Then we will review the numerical investigations performed to simulate those experiments.

A study of laminar shock wave/boundary layer interaction with separation has been executed in the R5Ch wind tunnel with a hollow cylinder flare [10, 12]. The upstream

flow Mach number was equal to 9.9. Visualizations by Electron Beam Fluorescence (EBF) and wall visualizations by oil flow have been done. Pressure and heat-flux have been measured along the cylinder flare. They could visualize the attached shock wave at the sharp leading edge and the separation shock wave. These two shocks converge above the end of the flare. The pressure coefficient decreased slowly on the upstream part of the cylinder. This decrease was followed by a two step compression. A first compression was due to the separation process and a second compression, far more important, occurred during reattachment. The heat flux decreased along the cylinder in the upstream part, where the flow was governed by the viscous interaction effects emanating from the leading edge. Further downstream, the evolution was characteristic of a laminar interaction with a large boundary layer separation.

A series of experiments was conducted in the Princeton University Mach 8 Wind Tunnel to study shock interactions on axisymmetric double-cone geometries. Two models, under low, and high Reynolds number conditions, were tested. The models were instrumented with pressure taps and thermocouples, and Schlieren images were taken. [55] The 25-35 degree doublecone generated a type VI shock interference as classified by Edney. [20]. As the second cone half angle was increased to 50 in the second model, a type VI interaction was no longer possible and a type V interference was visualized.

Holden et al. conducted experimental studies [29] over axisymmetric hollow cylinder/flare configurations and cone/cone models in LENS I facility at CUBRC in 2001. These experimental studies were conducted over a Mach number range from 9 to 11 for low Reynolds numbers to ensure that the flows remained fully laminar throughout the interaction regions. Detailed measurements of the distributions of heat transfer and pressure, as well as Schlieren photographs of the flow fields were obtained. Later in 2002, they performed an additional set of experiments [31] to evaluate the effects of vibrational nonequilibrium of nitrogen in the freestream, thereby providing a more accurate definition of the freestream properties.

Jagadeesh et al. investigated the unsteady laminar flow around double cones in the Shock Wave Research Center (SWRC) free piston driven shock tunnel at a nominal Mach number of 6.99 using multiple optical techniques [22]. The time resolved shock

structure oscillations in the flow field around double cones have been visualized at a nominal stagnation enthalpy of 4.8 MJ/kg. In addition flow visualization studies was also carried out using Schlieren and double exposure holographic interferometry in order to precisely locate the separation point and measure the separation length. Their results for 65, 68, and 70 degree second cone angles revealed severe shock oscillation and later movement of the transmitted shock impingement on the second cone surface. The non-linear behavior behavior of the shock interaction process was observed in their measurements. On the other hand, when the second cone angle was decreased to 50 degree, the flow field around the cone became steadier and the type V shock interference was observed.

In order to compare measurements in low and high enthalpy flows, Chanetz conducted experiments [11] in the R5Ch wind tunnel at ONERA Meudon [5] at cold and hot hypersonic flow. The test cases were a purely laminar low enthalpy interaction performed at Mach number 9.92; and a high enthalpy interaction performed at Mach 9.4 over a hollow cylinder flare model. The flow was visualized using EBF [26] and the wall pressure measurements were executed with variable reluctance differential transducers and the heat fluxes determined from the surface temperature rise using platinum films. In addition, density and specific mass measurements were performed using electron beam X-ray techniques [26]

Swantek and Austin investigated heat transfer and flowfield structure of hypersonic flows of air and nitrogen over a $30 - 55^\circ$ double wedge [50]. An expansion tube at the University of Illinois hypersonic facility was used to generate air and nitrogen flows with stagnation enthalpies ranging from 2.1-8 MJ/kg and Mach numbers from 4 to 7. Measurements were made using fast response coaxial thermocouples and Schlieren images were obtained.

In more recent experimental studies [40] conducted in LENS XX expansion tunnel [3], Holden et al. obtained detailed heat flux and pressure measurements in laminar separated regions of shock wave/boundary layer interaction for a range of total enthalpies from 5.44 MJ/kg to 21.77 MJ/kg in air, nitrogen, and oxygen using two models - the $25^\circ/55^\circ$ double cone and 30° hollow cylinder. In both geometries, shock

induced pressure rise caused by a corner compression produced separation and interaction between shocks and the laminar boundary layer.

Comparisons of the DSMC and Navier-Stokes codes [44] for the hollow cylinder flare configuration were made with the results of experimental measurements [10, 12] conducted in the ONERA R5Ch wind tunnel for heating, pressure, and extent of separation. Agreement between computations and measurements for various quantities were good except for pressure. Also results from the Navier-Stokes calculations suggested that the flow for the highest density double cone case may be unsteady; however, the DSMC solution did not show evidence of unsteadiness.

The comparisons between the experiments and the computations performed by Wright et al. [55] was in good agreement for the Type VI shock interaction, although the computations slightly over predicted the location of the reattachment point for Type V shock interactions.

A CFD code validation exercise [33, 25, 35, 24, 13, 9] was conducted as part of the activity of the RTO/AVT Working Group No 10 and with AFOSR support in which the two hypersonic flow configurations measured in previous experimental investigations [28, 29] were studied. Generally the DSMC method did not yield results that were as good as Navier-Stokes methods. This was in part because the flows were very dense. Also for complex dense flows there were doubts about how well converged the solutions were. Additionally, it was evident that the Navier-Stokes methods consistently over predicted the heat transfer on the forebody ahead of separation point. Later Nompelis et al. investigated the source of this discrepancy by including the effects of vibrational nonequilibrium, slip at the model surface, and weak flow nonuniformity in the test section [46, 45]. These simulations showed an improvement in the size of the separation zone and the heat transfer, but their further grid refinement did not agree well with the experimental results. A detailed and careful effort was made by Gallis et al. to address the numerical accuracy of their Navier-Stokes, and DSMC simulations [8]. The results obtained indicated that the failure of their earlier DSMC simulations was due to insufficient grid refinement within the recirculation zone. Furthermore, it was concluded that accurate simulations of the double cone experimental conditions with

the DSMC methods was not possible due to extreme computational cost. A systematic study of the effects of the numerics on the simulation of a steady hypersonic flow past a sharp double cone was performed by Druguet et al. [18]. They showed that the computed flowfield is very sensitive to the numerical flux evaluation method and slope limiter used. They found that, when the grid is fine enough, all of the flux evaluation schemes give the same results, though this might require a very large number of points for the most dissipative schemes.

A combined numerical and experimental analysis of hypersonic flow over heated compression ramps and double wedge configurations with various nose radii was conducted in [47, 7]. Different surface temperatures were specified to investigate the effect of an entropy layer behind a blunt leading edge on the structure of the flowfield. Their results indicated an ambiguous effect of the leading edge bluntness on the size of separation.

Kirk et al. simulated the wind tunnel experiments for the hollow cylinder flare and double cone configurations [30, 53] as a CFD validation exercise [34]. While in both cases the model and numerical method were found to be in general agreement, there was discrepancy in the experimentally measured separation location in the case of hollow cylinder flare.

Bibin et al. developed a two dimensional finite volume based CFD solver and implemented it to study the effect of various flow and geometric parameters on the ramp induced SWBLI in laminar hypersonic flows [6]. They studied the effect of ramp angle on shock induced boundary layer separation and enumerated the observations on Marini [43] to find that the correlation for predicting incipient separation works well only for well separated flows. The effect of leading edge bluntness on separation dynamics showed that the flow is laminar only up to the point of separation and supported the experimental observations of possible turbulent reattachment.

A series of independent computations [37] were performed by researchers in the US and Europe for two generic configurations (a double cone in N_2 and a cylinder in air with significant freestream atomic O) and compared with experimental data for surface pressure and heat transfer. For the higher enthalpy double cone configuration (Run

42), the computations and experiment displayed close agreement. Moreover, both the experiment and all computations indicated that the flowfield was steady for this case. Surprisingly, all simulations predict a dramatically unsteady flow for the low enthalpy double cone configuration (Run 40) in direct contrast to the experiment where the flowfield was observed to achieve steady state. Consequently, an additional experiment (Run 80) was performed at nearly the same enthalpy but the Reynolds number was reduced by an approximate factor of two. The computed flowfield for this case was observed to be steady in agreement with experiment, and the computed surface pressure and heat transfer displayed close agreement with experiment. The predicted heat transfer and surface pressure for the low enthalpy cylinder were in good agreement with experiment. For the high enthalpy cylinder case, the predicted pressure profiles showed close agreement with experiment while the predicted heat transfer underpredicted the experiment, thus indicating the need for accurate modeling of the effects of surface catalycity.

Komives et al. simulated selected cases of Swantek double wedge experiments [50] using US3D [38]. Their two dimensional simulations predicted an unsteady separation and shock-shock interaction under both reacting and non-reacting conditions. Their three dimensional simulations also showed nonuniformities in the wedge boundary layer during flow development.

1.3 Scope of the Thesis

In spite of the decades of research into hypersonic flow, there are still many challenges to analyzing and designing high speed vehicles. Recent failures such as the Columbia accident are clear evidence that there are still many unknown parameters in the field of hypersonic flight that even our best experimental or numerical capabilities can not adequately predict. Specifically, for high enthalpy states of flight vehicles, there is tremendous uncertainty in CFD ability to model chemical reactions, as well as predicting flow features. Moreover, there is additional work left to be done before CFD predictions of hypersonic shock/ boundary layer interaction will be fully grid independent. The objective of this thesis is to fill this gap by assessing CFD capability for

prediction of heat transfer and pressure in laminar shock wave-boundary layer interaction using the perfect gas Navier-Stokes equations for a series of hypersonic shock-wave boundary layer experiments performed at the Calspan University of Buffalo Research Center (CUBRC).

Chapter 2

Description of Experiment

2.1 Introduction

In this chapter we present the experiments performed in the LENS XX expansion tunnel at the Calspan University of Buffalo Research Center (CUBRC). Detailed surface heat flux and pressure measurements have been made in laminar separated regions of shock wave/boundary layer interaction in high-enthalpy flows over double cone and hollow cylinder/flare configurations. The major objective of the experimental program was to study real gas effects on the scale and distribution of heat flux and pressure to assess the models of gas chemistry and thermodynamic interactions employed in CFD simulations. The experimental dataset and comparisons with blind submissions using a number of popular hypersonic Navier-Stokes CFD codes were presented [41] at the AIAA Aviation 2014 Fluid Dynamics meeting in Atlanta, GA on June 2014.

2.2 LENS XX Facility

Hypervelocity ground test facilities are essential to the development and advancement of hypersonic reentry vehicles. There is a serious lack of well-characterized, clean flow, truly high-enthalpy facilities capable of generating reentry type velocity flows. LENS XX was designed to fill in this gap and provide a capability for larger scale hypervelocity testing. LENS XX is a large-scale expansion tunnel that can be operated over a large range of conditions with little or no test gas dissociation. Figure 2.1 is a schematic of LENS XX along with a representative $x - t$ diagram. As can be seen in Figure 2.1, LENS XX consists of three sections (a driver, driven and expansion section) separated by two diaphragms. A full description of the gas dynamics processes involved in expansion

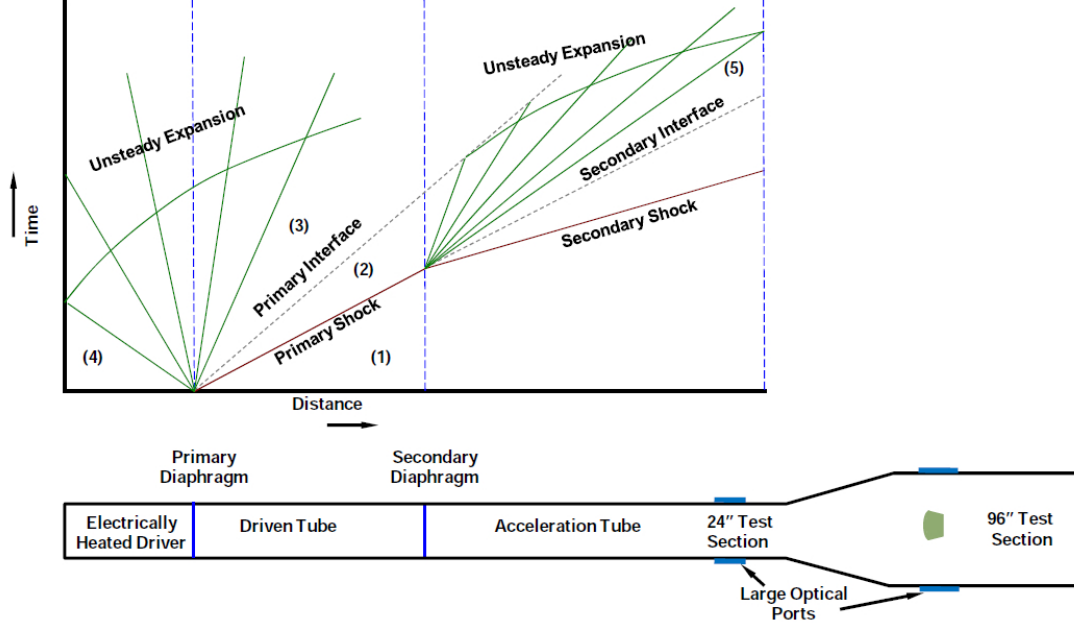


Figure 2.1: Representative $x - t$ diagram and schematic of LENS XX [19]

tunnel operation can be found in [2, 51, 49]. There are several key features that make LENS XX stand apart from other high enthalpy facilities. First of all, the driver section is electrically heated with hydrogen as the driver gas. This feature doubles the sound speed of the driver which allows testing at higher enthalpy conditions. Free piston tunnels and combustion driven tunnels generate soot and have some uncertainty in exact driver gas conditions. The quiescent driver gas in LENS XX is ideal for generating well understood clean flow conditions. The primary diaphragm uses a double diaphragm system for test condition repeatability. The long length greatly increases test time compared with other facilities of this type, and the large diameter generates a much larger coreflow with minimal viscous/boundary layer effects. The secondary diaphragm station is movable for tailoring of the test condition to obtain the longest possible test time. Characterization of the facility is done by using shock speed measurements, pitot probe profiles, freestream pressure probes, and Schlieren analysis along with numerical codes.

2.3 DoubleCone Experiments

The experimental program was conducted principally in LENS XX expansion tunnel using dry air as a test gas (assumed to consist of 76.5% N_2 and 23.5% O_2 by mass) at total enthalpies from 5 MJ/kg to 21 MJ/kg to evaluate real gas effects on the characteristics of the interaction regions.

Two new models were constructed and instrumented for the test program conducted principally in LENS XX. These models incorporated new high frequency pressure instrumentation required to accurately follow the establishment of the separated interaction region at the junction between the forebody and the flare on the models in the approximately 1 ms run time of LENS XX. A photograph and schematic diagram of the double cone configuration is shown in Figure 2.2. Pressure and heat transfer instrumentation Figure 2.2(a) were incorporated in the model to accurately record the flowfield development over the double cone configuration with semi-angles of 25° and 55° Figure 2.2(b).

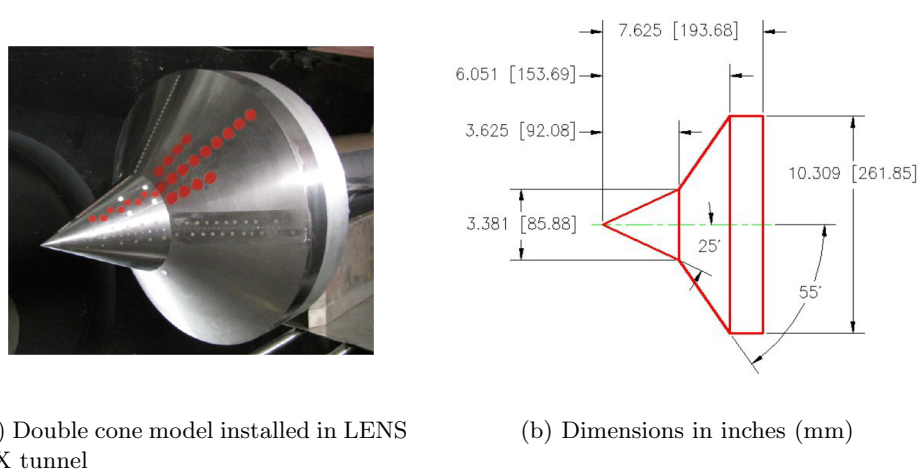


Figure 2.2: Double cone configuration

During the preparation for the program, calibration studies was performed in LENS XX involving rake surveys and measurements on hemispherical and cylindrical nose shapes in air under conditions similar to those used for hollow cylinder flare and double cone models. Based on these surveys, run conditions were selected to give well-defined

separated regions on the models and variations in the separated region lengths as functions of Reynolds number and total enthalpy. The measurement conditions for double cone selected cases are listed in Table. 2.1. These test conditions were generated using the CHEETAh code [42], where it may be assumed that the gas is in thermal equilibrium in the freestream, e.g. all thermal modes are in equilibrium with temperature and the test gas is in chemical equilibrium. Because of the short runtime of the facility, the wall surface temperature is assumed constant at 300 K.

The flowfield for all four experimental cases was judged to be laminar and steady [41].

Run No.	Total Enthalpy (MJ/kg)	Mach Number	Pitot Pressure (kPa)	Unit Reynolds Number / $10^6(1/m)$	Velocity (km/s)	Density (g/m^3)	Temperature (K)
1	5.44	12.2	5.1	0.14	3.246	0.499	175
2	9.65	10.90	17.5	0.19	4.303	0.984	389
4	21.77	12.82	39.5	0.20	6.497	0.964	652
6	15.23	11.46	59.0	0.39	5.466	2.045	573

Table 2.1: Freestream conditions for double cone experiments

Chapter 3

Mathematical Formulation

In this chapter, we review the set of partial differential equations that are chosen describe the dynamics of the flow field. The basic assumption is that the flowfield is fully laminar and compressible, and the gas is perfect.

3.1 Perfect Gas Laminar Navier-Stokes

The governing equations are the laminar Navier-Stokes equations for a perfect gas. Using the Einstein summation notation,

$$\frac{\partial \rho}{\partial t} + \frac{\partial \rho u_j}{\partial x_j} = 0 \quad (3.1)$$

$$\frac{\partial \rho u_i}{\partial t} + \frac{\partial \rho u_i u_j}{\partial x_j} = -\frac{\partial p}{\partial x_i} + \frac{\partial \tau_{ij}}{\partial x_j} \quad (3.2)$$

$$\frac{\partial \rho \varepsilon}{\partial t} + \frac{\partial}{\partial x_j} (\rho \varepsilon + p) u_j = -\frac{\partial q_j}{\partial x_j} + \frac{\partial \tau_{ij} u_i}{\partial x_j} \quad (3.3)$$

$$p = \rho R T \quad (3.4)$$

where u_i are the Cartesian velocity components, ρ is the density, and the total energy per unit mass ε is

$$\varepsilon = e + \frac{1}{2} u_j u_j \quad (3.5)$$

where the internal energy per unit mass e is

$$e = c_v T \quad (3.6)$$

and the heat flux vector and laminar viscous stress tensor are

$$q_j = -k \frac{\partial T}{\partial x_j} \quad (3.7)$$

$$\tau_{ij} = -\frac{2}{3} \mu \frac{\partial u_k}{\partial x_k} \delta_{ij} + \mu \left(\frac{\partial u_i}{\partial x_j} + \frac{\partial u_j}{\partial x_i} \right) \quad (3.8)$$

The molecular viscosity μ is defined by Sutherland's Law and the molecular Prandtl number $Pr = \mu c_p / k$ is 0.72. The gas constant $R = 287 \text{ J/kg}\cdot\text{K}$ for air.

3.1.1 Boundary Conditions

For viscous cases, the double cone boundary type is no slip with isothermal surface at 300 (K). Inflow and upper boundaries are fixed at freestream conditions, while the outflow has been set to zero gradient boundary condition.

3.2 The Numerical Method

The commercial flow solver GASpEx [1] was used. Run 1, and 2 were computed using Van Leer's flux-vector splitting [52] and second order upwind reconstruction [36] with Min-Mod limiter. Run 4, and 6 were computed using Roe [48] with Harten modification and the same reconstruction and limiter as the former. For all the Runs, time integration was performed using implicit dual time stepping [54].

3.3 Grid Generation

Two structured multiblock grids were generated using Matlab. The grid which was used for Run 1 and 2 of Table 2.1 consisted of 4,530,330 cells, and the grid used for Run 4 and 6 of Table 2.1 consisted of 1,332,320 cells. Very fine mesh was incorporated near the surface of the doublecone in order to capture the details of the shock-boundary layer interaction. Grid sequencing information is shown in Table 3.1.

Run Number	Sequence	Grid	Total Number of Cells
1	1	Coarse	291,600
	2	Medium	1,233,630
	3	Fine	4,530,330
2	1	Coarse	291,600
	2	Medium	1,233,630
	3	Fine	4,530,330
4	1	Coarse	333,080
	2	Medium	1,332,320
6	1	Coarse	333,080
	2	Medium	1,332,320

Table 3.1: Grid Sequences

3.4 Solution Schemes

The computations for Run 1, and 2 were performed using Van Leer flux splitting. Calculations for Run 4, and Run 6 were performed using Roe's method. Run 1 was computed using steady state analysis, and the rest were computed using transient schemes. The temporal integration for transient analysis is implicit double precision [36].

3.4.1 Finite Volume Method

The perfect gas Navier-Stokes equations can be written in vector form as

$$\frac{\partial Q}{\partial t} + \frac{\partial E}{\partial x} + \frac{\partial F}{\partial y} + \frac{\partial G}{\partial z} = \frac{\partial R}{\partial x} + \frac{\partial S}{\partial y} + \frac{\partial T}{\partial z} \quad (3.9)$$

where

$$Q = \begin{Bmatrix} \rho \\ \rho u \\ \rho v \\ \rho w \\ \rho \varepsilon \end{Bmatrix}, \quad E = \begin{Bmatrix} \rho u \\ \rho uu + p \\ \rho uv \\ \rho uw \\ \rho \varepsilon u + pu \end{Bmatrix}, \quad F = \begin{Bmatrix} \rho v \\ \rho u v \\ \rho vv + p \\ \rho vw \\ \rho \varepsilon v + pv \end{Bmatrix}, \quad G = \begin{Bmatrix} \rho w \\ \rho uw \\ \rho vw \\ \rho ww + p \\ \rho \varepsilon w + pw \end{Bmatrix} \quad (3.10)$$

and

$$R = \begin{Bmatrix} 0 \\ \tau_{xx} \\ \tau_{xy} \\ \tau_{xz} \\ \beta_x - q_x \end{Bmatrix}, \quad S = \begin{Bmatrix} 0 \\ \tau_{xy} \\ \tau_{yy} \\ \tau_{yz} \\ \beta_y - q_y \end{Bmatrix}, \quad T = \begin{Bmatrix} 0 \\ \tau_{xz} \\ \tau_{yz} \\ \tau_{zz} \\ \beta_z - q_z \end{Bmatrix} \quad (3.11)$$

where

$$\begin{aligned} \beta_x &= \tau_{xx}u + \tau_{xy}v + \tau_{xz}w \\ \beta_y &= \tau_{xy}u + \tau_{yy}v + \tau_{yz}w \\ \beta_z &= \tau_{xz}u + \tau_{yz}v + \tau_{zz}w \end{aligned} \quad (3.12)$$

and q and τ are defined as in Eqs. 3.7 and 3.8.

Using a coordinate transformation $(x, y, z) \rightarrow (\xi, \eta, \zeta)$ the governing equations become

$$\frac{\partial Q'}{\partial t} + \frac{\partial E'}{\partial \xi} + \frac{\partial F'}{\partial \eta} + \frac{\partial G'}{\partial \zeta} = \frac{\partial R'}{\partial \xi} + \frac{\partial S'}{\partial \eta} + \frac{\partial T'}{\partial \zeta} \quad (3.13)$$

Denote a finite volume cell by indices i, j and k , respectively in the ξ, η and ζ directions. Integrating the above equations over a cell yields

$$\begin{aligned} \frac{d(Q'_{ijk} V_{ijk})}{dt} + (E'_{i+\frac{1}{2}} - E'_{i-\frac{1}{2}}) + (F'_{j+\frac{1}{2}} - F'_{j-\frac{1}{2}}) + (G'_{k+\frac{1}{2}} - G'_{k-\frac{1}{2}}) = \\ (R'_{i+\frac{1}{2}} - R'_{i-\frac{1}{2}}) + (S'_{j+\frac{1}{2}} - S'_{j-\frac{1}{2}}) + (T'_{k+\frac{1}{2}} - T'_{k-\frac{1}{2}}) \end{aligned} \quad (3.14)$$

where Q_{ijk} is the volume-averaged value of the vector Q and V_{ijk} is the volume of the cell (i, j, k) . It is assumed that $\Delta\xi = \Delta\eta = \Delta\zeta = 1$ without loss of generality. The term $E'_{i+\frac{1}{2}}$ indicates evaluation of the flux E' on the positive ξ -face of the cell identified by its indices (i, j, k) . Similarly, term $E'_{i-\frac{1}{2}}$ indicates evaluation of the flux E' on the negative ξ -face of the cell identified by its indices (i, j, k) . A similar notation applies to the fluxes on the positive and negative η - and ζ -faces. Here

$$E' = \frac{1}{J} \begin{Bmatrix} \rho u' \\ \rho uu' + \xi_x p \\ \rho vu' + \xi_y p \\ \rho wu' + \xi_z p \\ (\rho\varepsilon + p)u' \end{Bmatrix}, \quad F' = \frac{1}{J} \begin{Bmatrix} \rho v' \\ \rho uv' + \eta_x p \\ \rho vv' + \eta_y p \\ \rho wv' + \eta_z p \\ (\rho\varepsilon + p)v' \end{Bmatrix}, \quad G' = \frac{1}{J} \begin{Bmatrix} \rho w' \\ \rho uw' + \zeta_x p \\ \rho vw' + \zeta_y p \\ \rho ww' + \zeta_z p \\ (\rho\varepsilon + p)w' \end{Bmatrix} \quad (3.15)$$

and

$$\begin{aligned}
R' &= \frac{1}{J} \left\{ \begin{array}{l} 0 \\ \xi_x \tau_{xx} + \xi_y \tau_{xy} + \xi_z \tau_{xz} \\ \xi_x \tau_{xy} + \xi_y \tau_{yy} + \xi_z \tau_{yz} \\ \xi_x \tau_{xz} + \xi_y \tau_{yz} + \xi_z \tau_{zz} \\ \xi_x \beta_x + \xi_y \beta_y + \xi_z \beta_z \end{array} \right\}, \\
S' &= \frac{1}{J} \left\{ \begin{array}{l} 0 \\ \eta_x \tau_{xx} + \eta_y \tau_{xy} + \eta_z \tau_{xz} \\ \eta_x \tau_{xy} + \eta_y \tau_{yy} + \eta_z \tau_{yz} \\ \eta_x \tau_{xz} + \eta_y \tau_{yz} + \eta_z \tau_{zz} \\ \eta_x \beta_x + \eta_y \beta_y + \eta_z \beta_z \end{array} \right\}, \\
T' &= \frac{1}{J} \left\{ \begin{array}{l} 0 \\ \zeta_x \tau_{xx} + \zeta_y \tau_{xy} + \zeta_z \tau_{xz} \\ \zeta_x \tau_{xy} + \zeta_y \tau_{yy} + \zeta_z \tau_{yz} \\ \zeta_x \tau_{xz} + \zeta_y \tau_{yz} + \zeta_z \tau_{zz} \\ \zeta_x \beta_x + \zeta_y \beta_y + \zeta_z \beta_z \end{array} \right\}
\end{aligned} \tag{3.16}$$

and defining

$$\begin{aligned}
u' &= \xi_x u + \xi_y v + \xi_z w \\
v' &= \eta_x u + \eta_y v + \eta_z w \\
w' &= \zeta_x u + \zeta_y v + \zeta_z w \\
J &= \frac{\partial(\xi, \eta, \zeta)}{\partial(x, y, z)}
\end{aligned} \tag{3.17}$$

where

$$\zeta_x = \frac{\partial \xi}{\partial x}, \text{etc} \tag{3.18}$$

The inviscid fluxes E' , F' and G' are represented by either Roe's method or Van Leer's method as discussed in the next section. The viscous and heat flux terms are represented by central differences.

3.4.2 Van Leer's Method

Calculations for run 1, and run 2 was performed using Van Leer's method. Van Leer [52] developed a flux-vector splitting algorithm based on Mach number. Here we explain Van Leer's method by considering a flux F across a cell face of unit area, where for simplicity the face is assumed perpendicular to the x -direction. The flux vector can be written as:

$$F = \begin{Bmatrix} \rho a M \\ \frac{\rho a^2}{\gamma} (\gamma M^2 + 1) \\ \rho u v \\ \rho u w \\ \rho a^3 M \left[\frac{1}{\gamma-1} + \frac{1}{2} M^2 \right] \end{Bmatrix} \quad (3.19)$$

The basic idea behind flux-vector splitting is to split the inviscid flux vector into two contributions based upon the eigenvalues of the flux Jacobian. For example, the inviscid flux vector is split as

$$F_{i+1/2} = F_{i+1/2}^+ + F_{i+1/2}^- \quad (3.20)$$

where all the eigenvalues of F^+ are positive and those of F^- are negative. Each of these parts can be evaluated using Q^l or Q^r as appropriate, where Q^l is the reconstructed value of Q to the left face of the cell, etc.

$$\begin{aligned} F_{i+1/2}^+ &= F^+(Q_{i+1/2}^l) \\ F_{i+1/2}^- &= F^-(Q_{i+1/2}^r) \end{aligned} \quad (3.21)$$

By design the flux-vector splitting sets the interface flux equal to the full flux for supersonic flow. That is:

$$\begin{cases} F^+(Q_{i+1/2}^l) = F(Q_{i+1/2}^l) & M > 1 \\ F^-(Q_{i+1/2}^r) = 0 & \\ \begin{cases} F^+(Q_{i+1/2}^l) = 0 & M < -1 \\ F^-(Q_{i+1/2}^r) = F(Q_{i+1/2}^r) & \end{cases} & \end{cases} \quad (3.22)$$

3.4.3 Roe's Method with Harten Modification

Calculations for run 4, and run 6 was performed using Roe's method. Roe developed an algorithm based on an exact solution to an approximation of the generalized Riemann problem. Here we explain Roe's methodology considering a flux F across a cell face of unit area, where for simplicity the face is assumed perpendicular to the x -direction.

The flux is:

$$F = \begin{Bmatrix} \rho \\ \rho u^2 + p \\ \rho uv \\ \rho uw \\ \rho \varepsilon u + pu \end{Bmatrix} \quad (3.23)$$

and the Jacobian is

$$A(Q) = \begin{Bmatrix} 0 & 1 & 0 & 0 & 0 \\ (\gamma - 1)q - u^2 & (3 - \gamma)u & (1 - \gamma)v & (1 - \gamma)w & (\gamma - 1) \\ -uv & v & u & 0 & 0 \\ -uw & w & 0 & u & 0 \\ -Hu + (\gamma - 1)uq & H - (\gamma - 1)u^2 & -(\gamma - 1)uv & -(\gamma - 1)uw & \gamma u \end{Bmatrix} \quad (3.24)$$

where $H = \varepsilon + \frac{p}{\rho}$ is the total enthalpy and $q = \frac{1}{2}(u^2 + v^2 + w^2)$

The flux is defined by

$$F = \frac{1}{2} \left\{ F_l + F_r + \tilde{R} |\tilde{\Lambda}| \tilde{L} (F_l - F_r) \right\} \quad (3.25)$$

Defining Roe variables as

$$\begin{aligned}
\tilde{u} &= \frac{\sqrt{\rho_l} u_l + \sqrt{\rho_r} u_r}{\sqrt{\rho_l} + \sqrt{\rho_r}} \\
\tilde{v} &= \frac{\sqrt{\rho_l} v_l + \sqrt{\rho_r} v_r}{\sqrt{\rho_l} + \sqrt{\rho_r}} \\
\tilde{w} &= \frac{\sqrt{\rho_l} w_l + \sqrt{\rho_r} w_r}{\sqrt{\rho_l} + \sqrt{\rho_r}} \\
\tilde{H} &= \frac{\sqrt{\rho_l} H_l + \sqrt{\rho_r} H_r}{\sqrt{\rho_l} + \sqrt{\rho_r}} \\
\tilde{a}^2 &= (\gamma - 1)[\tilde{H} - \frac{1}{2}(\tilde{u}^2 + \tilde{v}^2 + \tilde{w}^2)]
\end{aligned} \tag{3.26}$$

\tilde{R} is the matrix of right eigenvectors of A using Roe variables.

$$\tilde{R} = \left\{ \begin{array}{cccccc} 0 & 0 & 0 & 1 & 1 \\ 0 & 0 & \tilde{u} & \tilde{u} + \tilde{a} & \tilde{u} - \tilde{a} \\ \tilde{v} & 0 & \tilde{v} & \tilde{v} & \tilde{v} \\ 0 & \tilde{w} & \tilde{w} & \tilde{w} & \tilde{w} \\ \tilde{v}^2 & \tilde{w}^2 & \tilde{q} & \tilde{H} + \tilde{u}\tilde{a} & \tilde{H} - \tilde{u}\tilde{a} \end{array} \right\} \tag{3.27}$$

$\tilde{\Lambda}$ is the diagonal matrix of absolute value of eigenvalues of A using Roe variables.

$$\tilde{\Lambda} = \left\{ \begin{array}{cccccc} |\tilde{v}| & 0 & 0 & 0 & 0 \\ 0 & |\tilde{u}| & 0 & 0 & 0 \\ 0 & 0 & |\tilde{u}| & 0 & 0 \\ 0 & 0 & 0 & |\tilde{u} + \tilde{a}| & 0 \\ 0 & 0 & 0 & 0 & |\tilde{u} - \tilde{a}| \end{array} \right\} \tag{3.28}$$

\tilde{L} is the matrix of left eigenvectors of A using Roe variables.

$$\tilde{L} = \left\{ \begin{array}{ccccc} -1 & 0 & \frac{1}{\tilde{v}} & 0 & 0 \\ -1 & 0 & 0 & \frac{1}{\tilde{w}} & 0 \\ 1 - \frac{(\gamma-1)\tilde{q}}{\tilde{a}^2} & \frac{(\gamma-1)\tilde{u}}{\tilde{a}^2} & \frac{(\gamma-1)\tilde{v}}{\tilde{a}^2} & \frac{(\gamma-1)\tilde{w}}{\tilde{a}^2} & \frac{(\gamma-1)}{\tilde{a}^2} \\ \frac{(\gamma-1)\tilde{q}}{2\tilde{a}^2} - \frac{\tilde{u}}{2\tilde{a}} & -\frac{(\gamma-1)\tilde{u}}{2\tilde{a}^2} + \frac{1}{2\tilde{a}} & -\frac{(\gamma-1)\tilde{v}}{2\tilde{a}^2} & -\frac{(\gamma-1)\tilde{w}}{2\tilde{a}^2} & -\frac{(\gamma-1)}{2\tilde{a}^2} \\ \frac{(\gamma-1)\tilde{q}}{2\tilde{a}^2} + \frac{\tilde{u}}{2\tilde{a}} & -\frac{(\gamma-1)\tilde{u}}{2\tilde{a}^2} - \frac{1}{2\tilde{a}} & -\frac{(\gamma-1)\tilde{v}}{2\tilde{a}^2} & -\frac{(\gamma-1)\tilde{w}}{2\tilde{a}^2} & -\frac{(\gamma-1)}{2\tilde{a}^2} \end{array} \right\} \tag{3.29}$$

The Roe's flux-difference splitting scheme has been known to exhibit the carbuncle problem for blunt body flows, The Harten entropy fix corrects the lack of dissipation

at sonic points and at stagnation lines to prevent the carbuncle phenomena. The eigenvalues in Roe's scheme $|\tilde{\lambda}_i|$ are substituted by approximate values $|\hat{\lambda}_i|$

$$|\hat{\lambda}_i| = \begin{cases} \frac{\tilde{\lambda}_i^2}{4\epsilon\hat{a}} + \epsilon\hat{a} & \text{for } |\tilde{\lambda}_i| < 2\epsilon\hat{a} \\ |\tilde{\lambda}_i| & \text{for } |\tilde{\lambda}_i| \geq 2\epsilon\hat{a} \end{cases} \quad (3.30)$$

where $0 < \epsilon \leq \frac{1}{2}$ is a positive value and \hat{a} is a proper velocity scale, e.g. $\hat{a} = \tilde{a}$ [27]

3.5 The Limiter

The spatial discretization is second-order accurate with minimum modulus (min-mod) limiter. The min-mod function chooses the smaller of the two gradients (forward and backward) by magnitude if they have the same sign and zero otherwise. The function can be written as

$$\minmod(x, y) = \begin{cases} x & |x| < |y| \\ \text{and } xy > 0 \\ y & |y| < |x| \\ \text{and } xy > 0 \\ 0 & xy < 0 \end{cases} \quad (3.31)$$

3.6 Reconstruction

We need to know the primitive variables at the cell faces so that we can evaluate the fluxes. Reconstruction provides the link between the cell averages and the cell-face data. The reconstruction process simply converts known cell-average data into a pointwise field of data. The accuracy of reconstructing the primitive-variable field at the cell faces determines the spatial accuracy of the solution. A one-parameter family of interpolated values for the left state at the $i + \frac{1}{2}$ face and right state at the $i - \frac{1}{2}$ face can be represented as

$$\begin{aligned} Q_{i+\frac{1}{2}}^l &= Q_i + \frac{1}{4}[(1-\kappa)\nabla Q_i + (1+\kappa)\Delta Q_i] \\ Q_{i-\frac{1}{2}}^r &= Q_i - \frac{1}{4}[(1+\kappa)\nabla Q_i + (1-\kappa)\Delta Q_i] \end{aligned} \quad (3.32)$$

where the value for κ determines the spatial accuracy of the reconstruction. The forward and backward difference operators are

$$\begin{aligned}\Delta &= Q_{i+1} - Q_i \\ \nabla &= Q_i - Q_{i-1}\end{aligned}\tag{3.33}$$

We have used second order, fully upwind scheme. For this scheme $\kappa = -1$ and the linear reconstruction's slope equals the fully upwind gradient, $Q_i - Q_{i-1}$.

3.7 Temporal Quadrature

Computations for run 1 was performed using steady state assumptions. The time integration of fluxes for run 2,3 and 4 was performed by dual-time-stepping. Withington et al [54] proposed an implicit formulation referred to as dual-time-stepping which attains arbitrary time accuracy while allowing implicit treatment of the fluxes and source terms. This method incorporates a second temporal derivative (a pseudo-time derivative) for converging the root of a time accurate discretization. Because time accuracy is maintained on the outer loop, popular implicit time-integration techniques which do not maintain temporal accuracy can be applied to the inner loop in pseudo-time. The implicit governing equations with a pseudo-time derivative become

$$\frac{\partial}{\partial \tau} \iiint \mathbf{Q} dV = - \left(\frac{\partial}{\partial t} \iiint_V \mathbf{Q} dV + \iint (\mathbf{F} - \mathbf{F}_v) \cdot \hat{\mathbf{n}} dS \right)^{m+1} \tag{3.34}$$

where m represents a discrete solution in pseudo-time, τ . The dual-time-stepping procedure iterates in pseudo-time to find the solution at the $n+1$ time level in real time, t . As the inner problem converges, the solution at level m approaches the solution at time level $n + 1$.

Chapter 4

Results and Discussions

In this chapter we present simulations of the doublecone experiments, and show comparisons between experimental measurements and numerical predictions.

4.1 Results

Computational results for Run 1 in Table 2.1 are presented in Fig. 4.1. The x axis is the horizontal distance measured from the edge of the first cone. Fig. 4.1(a) shows a surface pressure peak of 9 (kPa) at $x = 11$ cm, and a separation point at $x = 6.5$ cm. Fig. 4.1(b) shows a surface heat flux peak of $110 \text{ Watt}/\text{cm}^2$ at $x = 11$ cm , and a separation point at $x = 6.5$ cm. The points of peak heat transfer and pressure coincide. Figs. 4.1(a), and 4.1(b) show that perfect gas simulations of surface pressure and heat transfer agree well with the experimental data. The general trend and level of pressure and heat flux fluctuation after reattachment are also reproduced, but are not exactly matched.

The flowfield structure for Run 1 in Table 2.1 is illustrated in Fig. 4.2. Fig. 4.2(a) shows the entire flowfield. The oblique shock generated by the first cone strongly interacts with the detached shock generated by the second cone, and a transmitted shock is formed, which impinges on the surface downstream of the cone-cone juncture. The adverse pressure gradient at the cone-cone juncture causes the boundary layer to separate. The separated region that forms at the corner creates its own shock, which interacts with the bow shock. As can be observed from Fig. 4.2(c), a supersonic jet is formed along the surface of the second cone downstream of the impingement point, and it undergoes a series of compressions and expansions as can be seen in Fig. 4.2(b). The flow behind the strong bow shock is subsonic, and therefore the shape of the jet

influences the shock structure.

Computational results for Run 2 in Table 2.1 are presented in Fig. 4.3. Fig. 4.3(a) shows a surface pressure peak of 37 (kPa) at $x = 12\text{cm}$, and a separation point at $x = 4.5\text{ cm}$. Fig. 4.3(b) shows a surface heat flux peak of 380 Watt/cm^2 at $x = 12\text{ cm}$, and a separation point at $x = 4.5\text{ cm}$. The points of peak heat transfer and pressure coincide. The total size of separation bubble is overpredicted by the perfect gas simulations. The inconsistency between the perfect gas computations and experimental data necessitates further real gas simulations for more accurate prediction of the flow field for this case.

The flowfield structure for Run 2 is shown in Fig. 4.4 and suggests that the type of the interaction is very similar to type IV of Edney classification of shock/shock interferences [20]. Essentially, the compression/expansion waves are completely distinguishable from Fig. 4.4(b).

Computational results for Run 6 in Table 2.1 are presented in Fig. 4.5. Fig. 4.5(a) shows a surface pressure peak of 175 (kPa) at $x = 11\text{ cm}$, and a separation point at $x = 4.8\text{ cm}$. Fig. 4.5(b) shows a surface heat flux peak of 1900 Watt/cm^2 at $x = 11\text{ cm}$, and a separation point at $x = 4.8\text{ cm}$. The points of peak heat transfer and pressure coincide. The total size of the separation bubble is overpredicted by the perfect gas simulations. The inconsistency between the perfect gas computations and experimental data necessitates further real gas simulations for more accurate prediction of the flow field for this case.

Again type IV of Edney classification of shock/shock interferences [20] can be interpreted from flowfield structure for Run 6 in Fig. 4.6. Specifically, the existence of a supersonic jet embedded between two subsonic regions as shown in Fig. 4.6(c) highlights the characteristic feature of the type IV interaction.

Computational results for Run 4 in Table 2.1 are presented in Fig. 4.7. Fig. 4.7(a) shows a surface pressure peak of 81 (kPa) at $x = 11\text{ cm}$, and a separation point at $x = 4.8\text{ cm}$. Fig. 4.7(b) shows a surface heat flux peak of 1600 Watt/cm^2 at $x = 11\text{ cm}$, and a separation point at $x = 4.8\text{ cm}$. The points of peak heat transfer and pressure coincide. The total size of the separation bubble is overpredicted by the perfect gas simulations. The inconsistency between the perfect gas computations and experimental

data necessitates further real gas simulations for more accurate prediction of the flow field for this case.

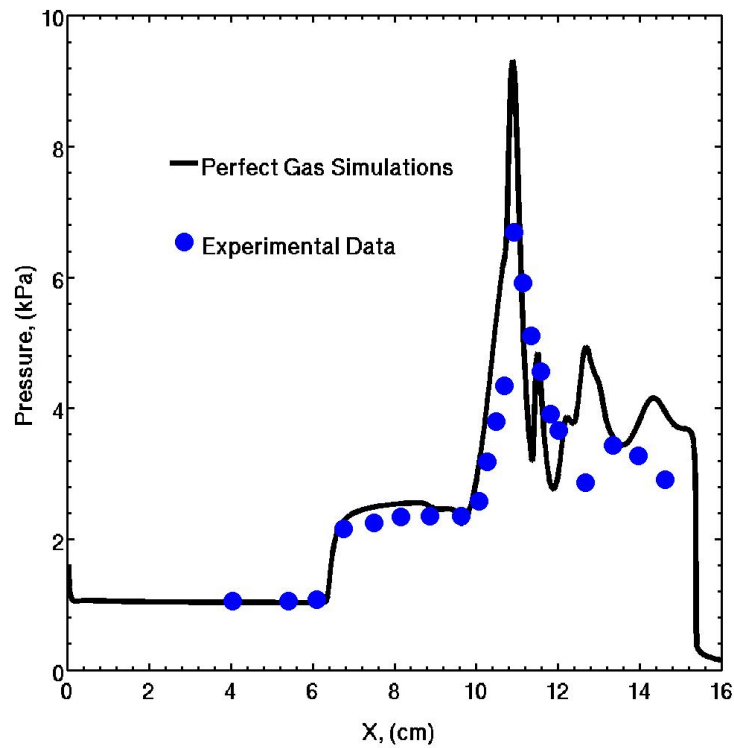
A closer look in the flowfield structure in Fig. 4.8 reveals that the type of interaction is still much like type IV. Here again the impingement of the supersonic jet bounded by two slip lines on the surface of doublecone as indicated in Fig. 4.8(c) results in the formation of a region of large pressure and heat transfer peaks observed in Fig. 4.8(b). For this case the shocks remain closer to the doublecone surface and the high pressure regions gets nearer to the wall.

4.1.1 Grid Refinement

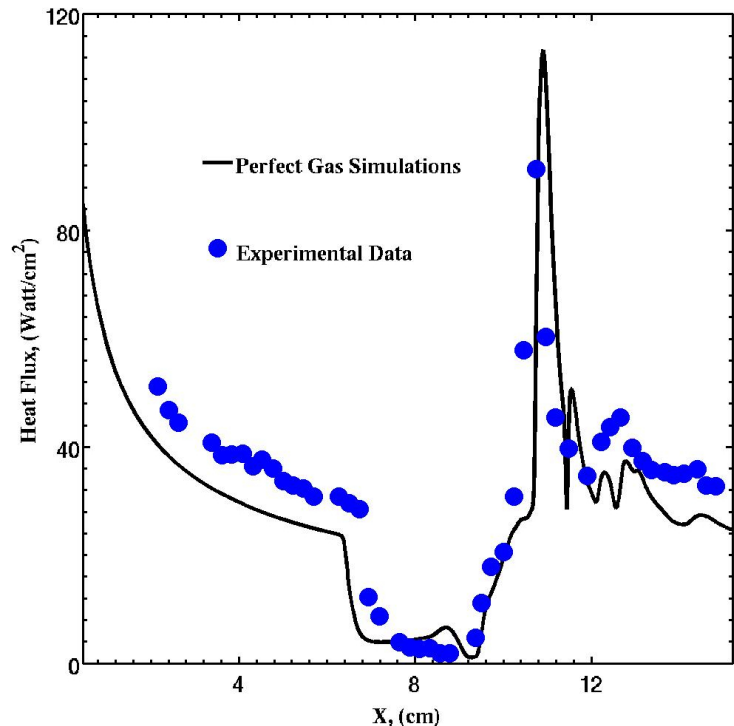
Additional perfect gas simulations were performed for Run 1, Table 2.1 using different sequences from Table 3.1. As it can be seen from Fig. 4.9, the difference in the computed surface pressure and heat transfer between the two grid levels is less than 5% which further confirms the grid independence of our simulations.

4.2 Discussions

In general, the size of the separation zone for Run 2, 4, and 6 is overpredicted. For these high enthalpy cases, the chemical processes that take place in the flow are tightly coupled with the fluid motion through energy exchange mechanisms. In these high enthalpy flows, dissociation takes place both in the high temperature region behind the bow shock, and inside the separation zone. In these regions, the highly energetic particles undergo collisions and lose some of their energy by causing dissociation of polyatomic species. By this process, energy is removed from the bulk flow and stored in the form of chemical energy. The rate at which this process takes place greatly impacts the mean flow. Thus, the size of the embedded region of separation is very sensitive to chemical effects in the flow. Therefore, a perfect gas model can not predict the size of separation zone, and subsequently the heat flux, and pressure profiles, for these high enthalpy cases since it completely neglects the existence of chemical processes.

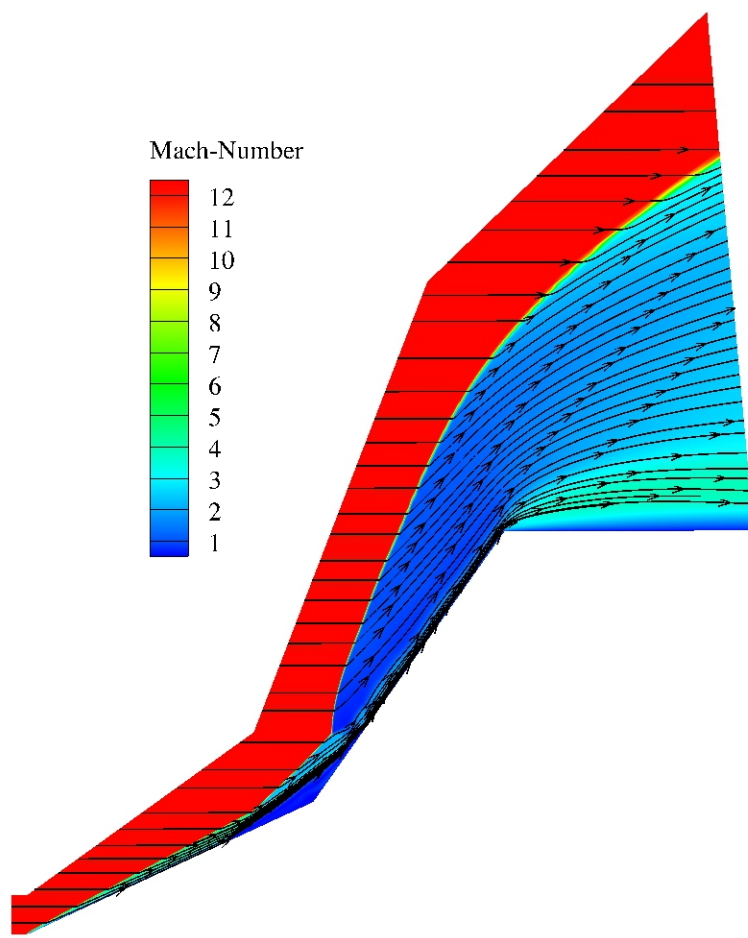


(a) Surface pressure



(b) Heat transfer rate

Figure 4.1: Computational results for Run 1, Table 2.1



(a) Overall flowfield

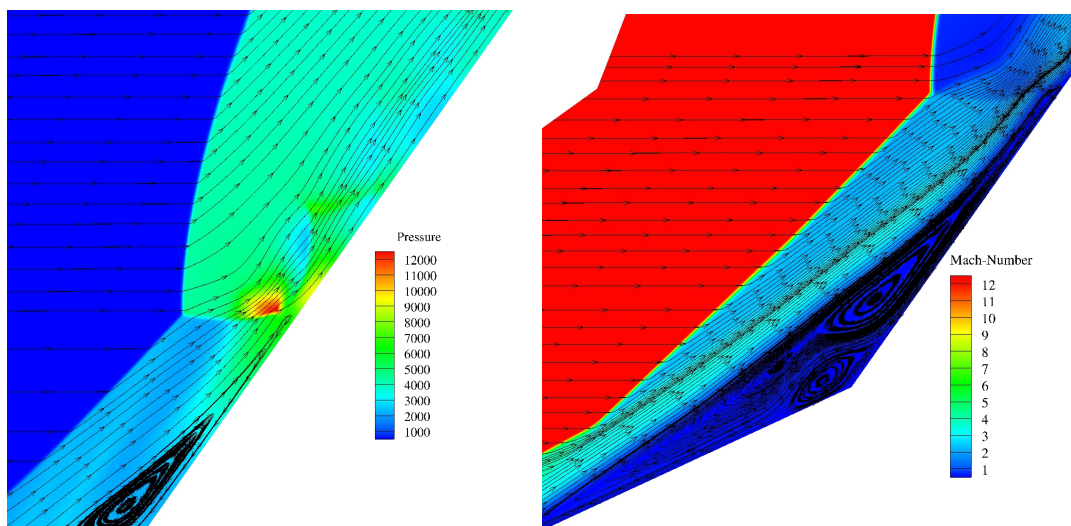
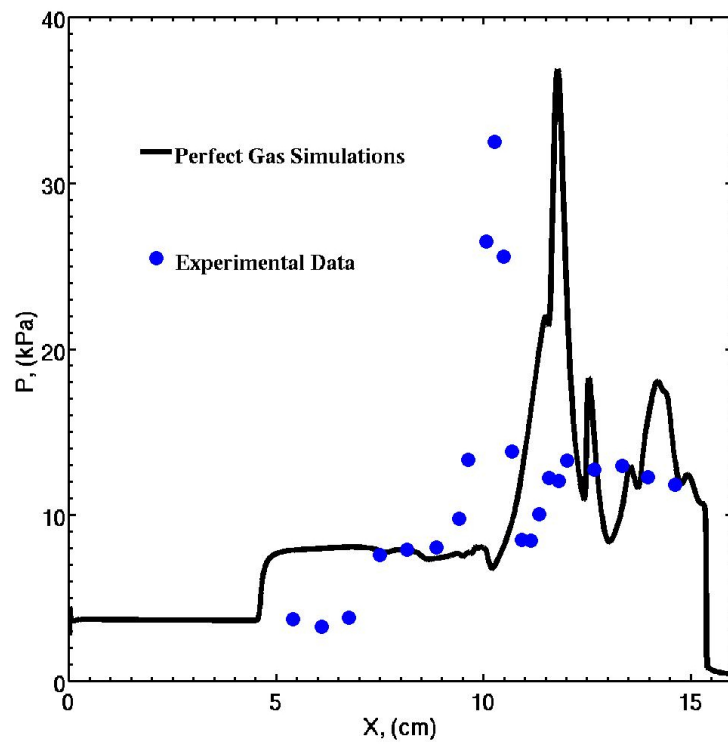
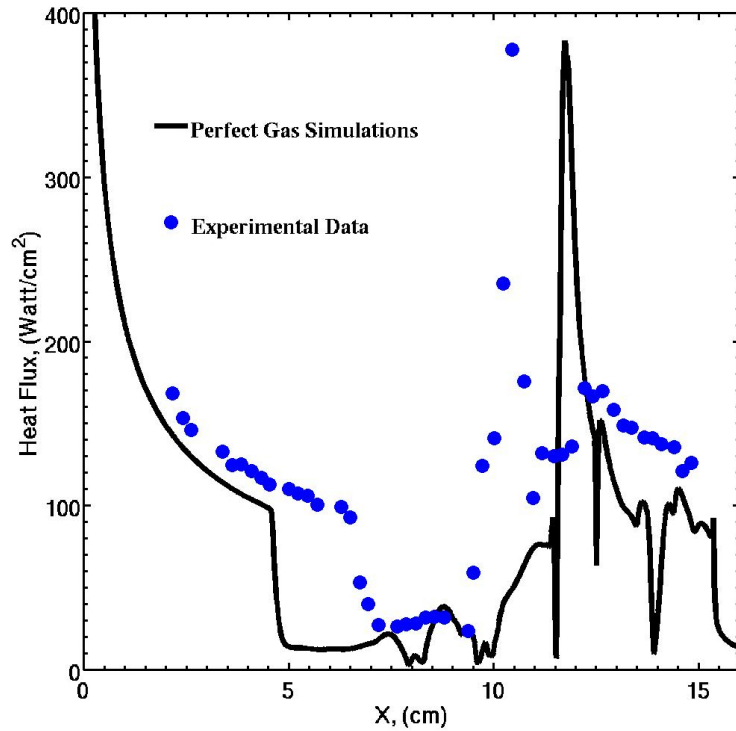


Figure 4.2: Flowfield structure for Run 1, Table 2.1

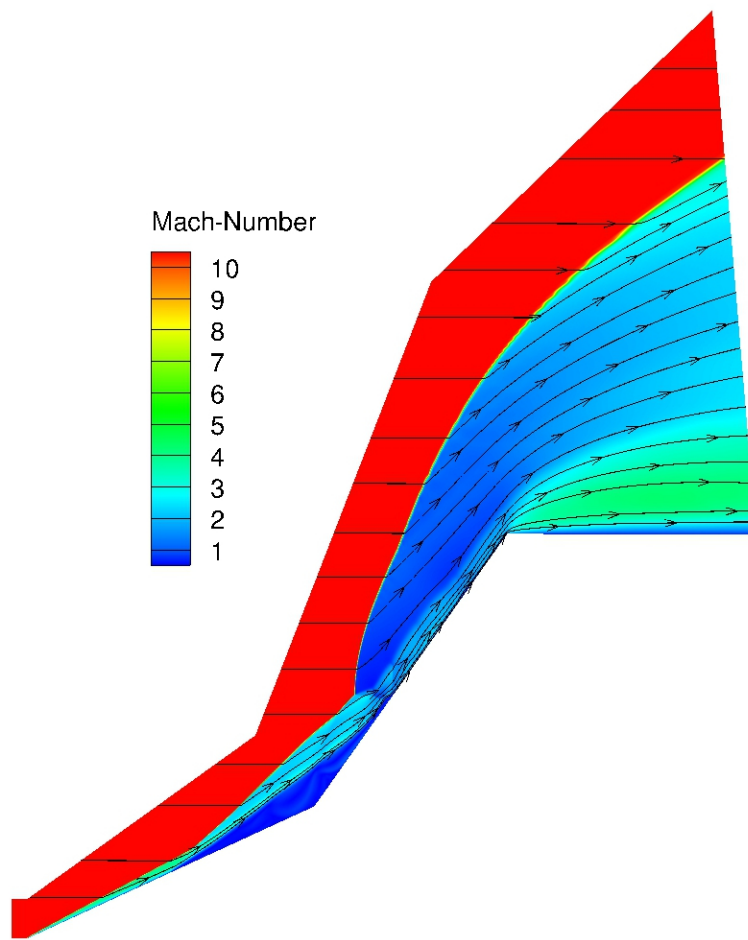


(a) Surface pressure

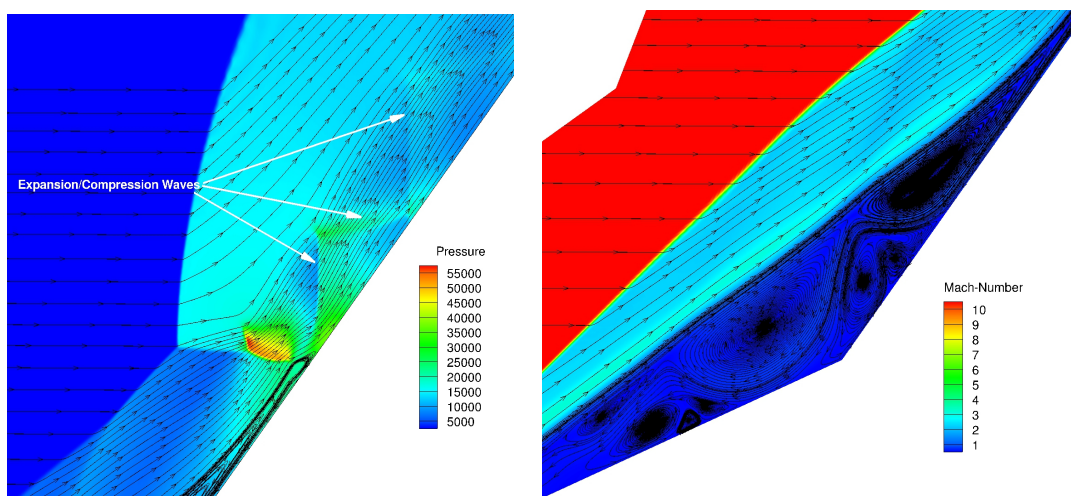


(b) Heat transfer rate

Figure 4.3: Computational results for Run 2, Table 2.1



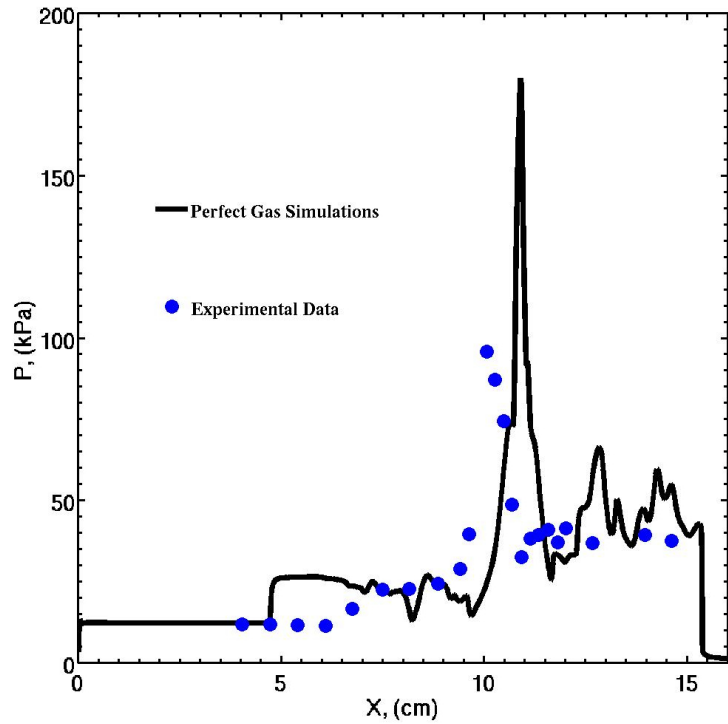
(a) Overall flowfield



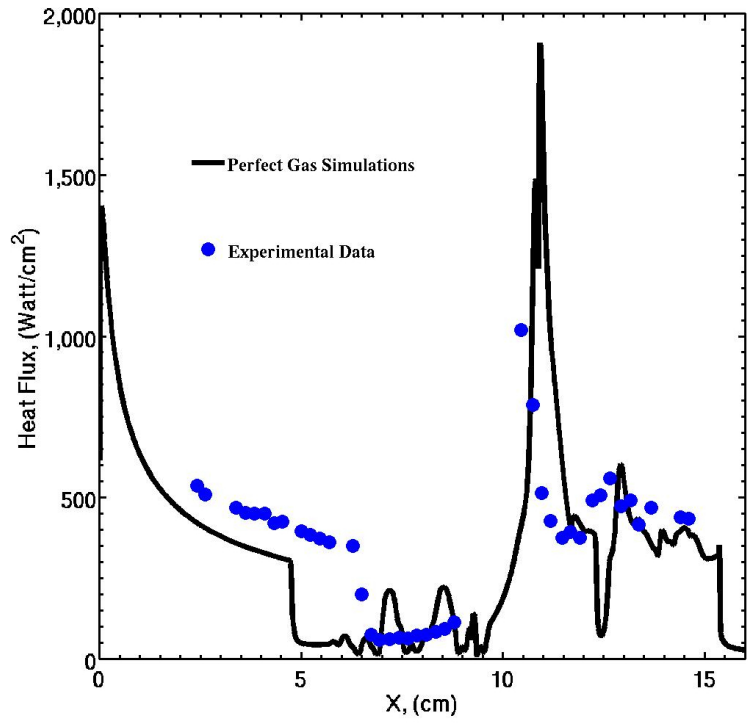
(b) Enlargement of flowfield

(c) Enlargement of flowfield

Figure 4.4: Flowfield structure for Run 2, Table 2.1

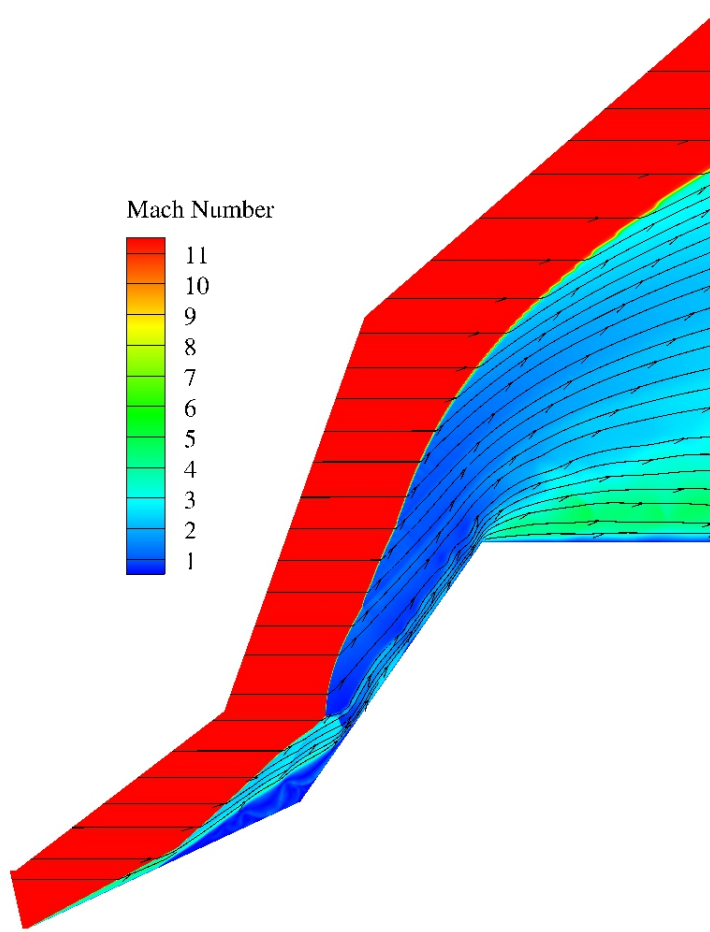


(a) Surface pressure



(b) Heat transfer rate

Figure 4.5: Computational results for Run 6, Table 2.1



(a) Overall flowfield

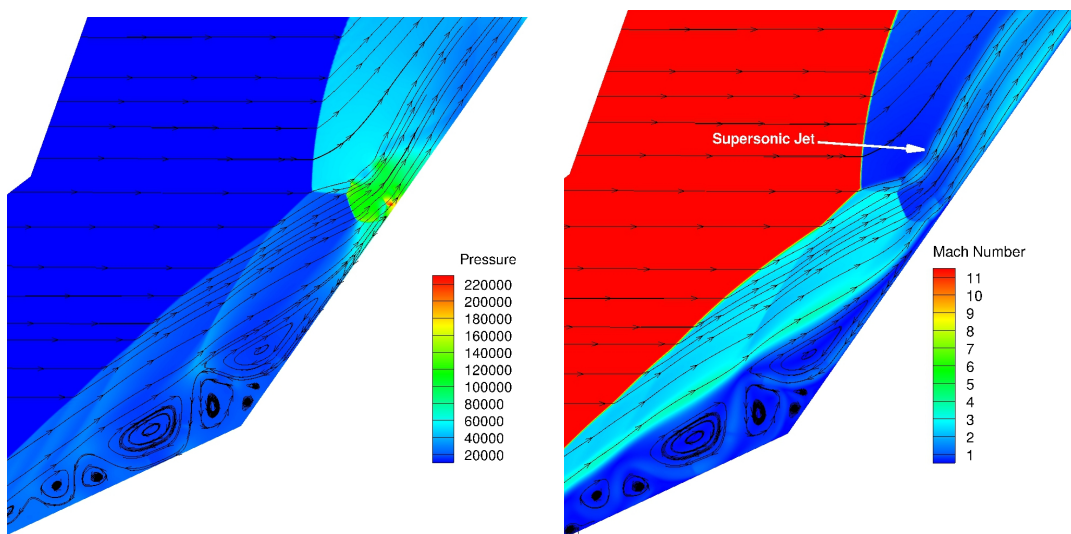
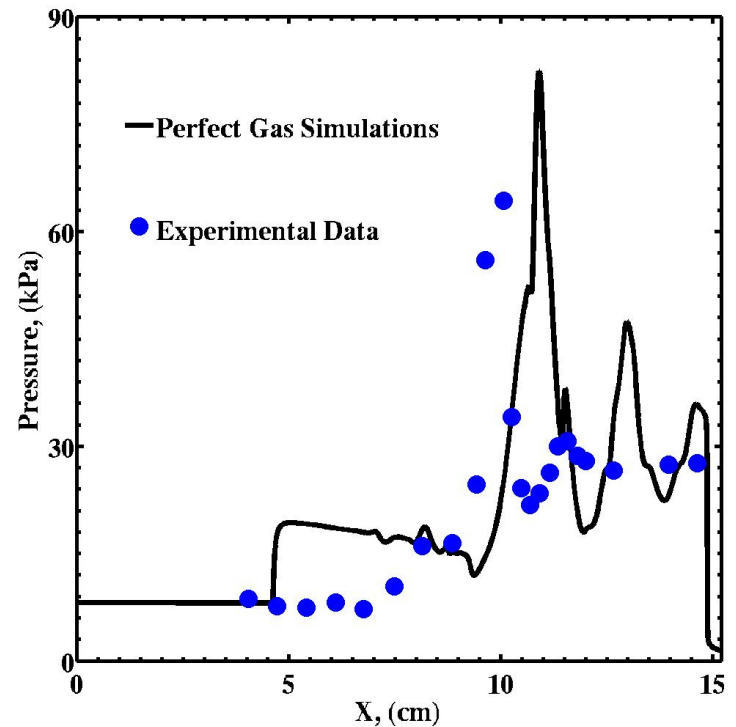
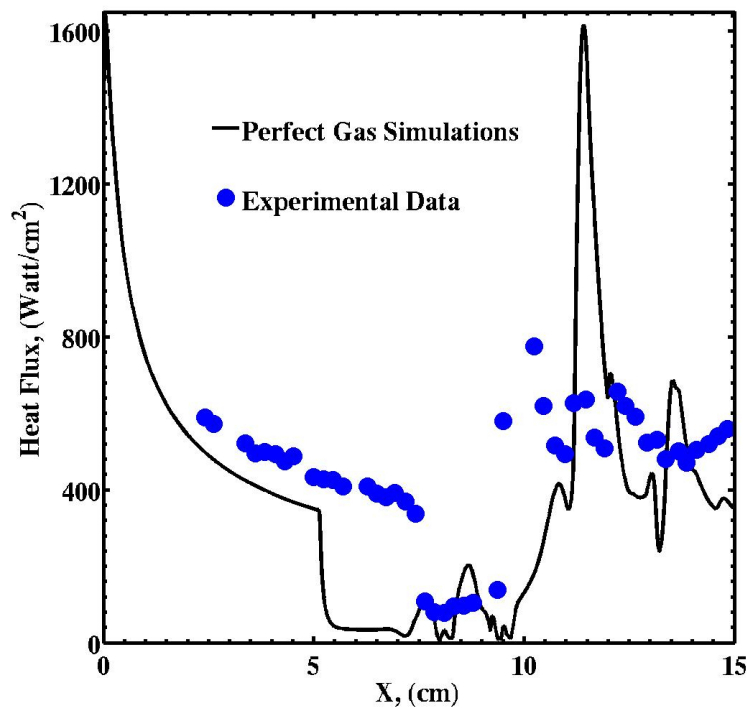


Figure 4.6: Flowfield structure for Run 6, Table 2.1



(a) Surface pressure



(b) Heat transfer rate

Figure 4.7: Computational results for Run 4, Table 2.1

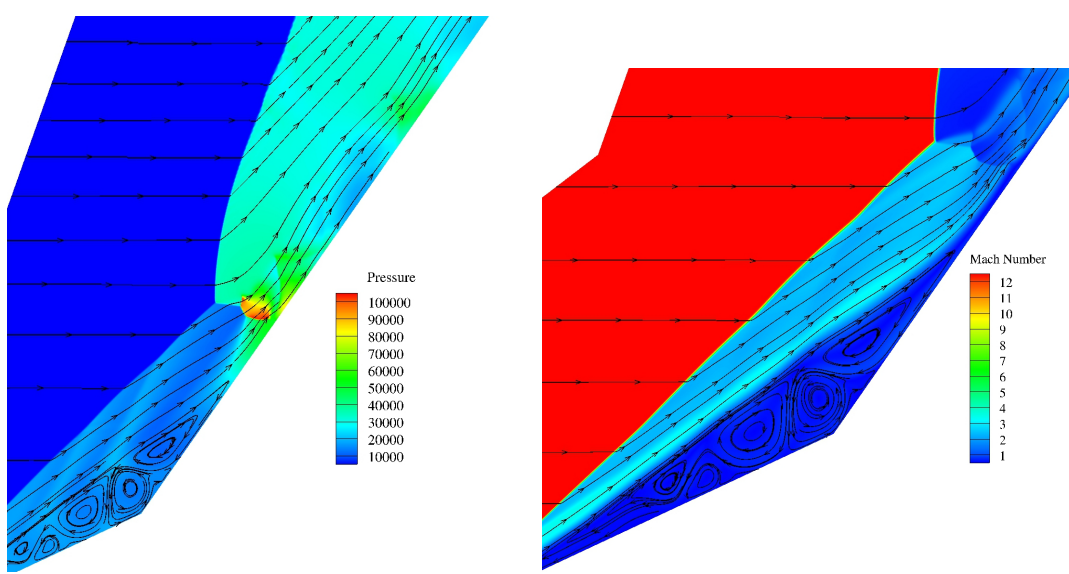
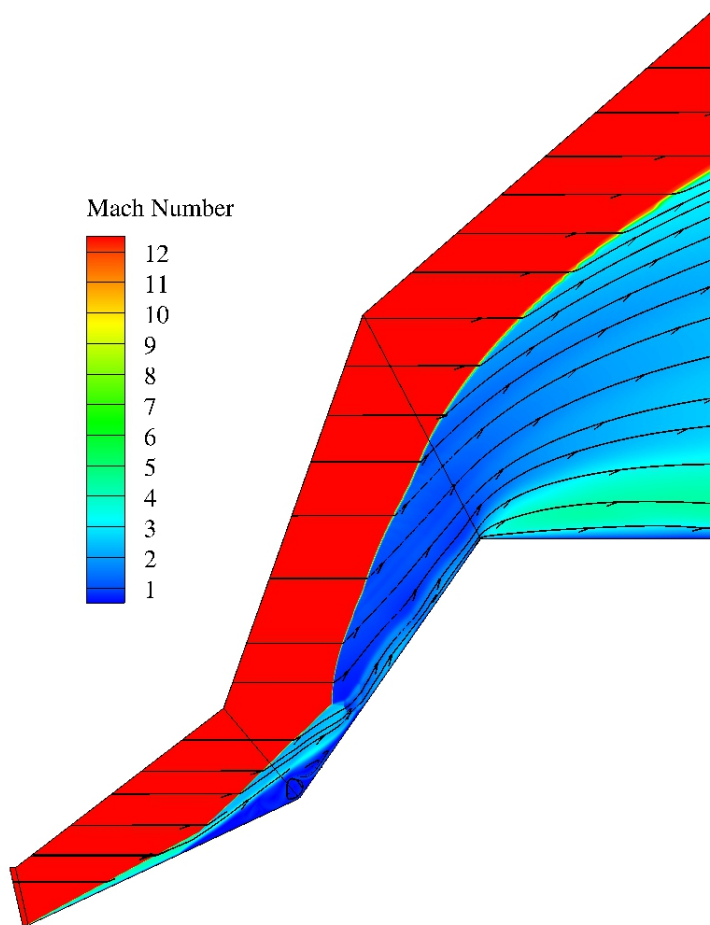
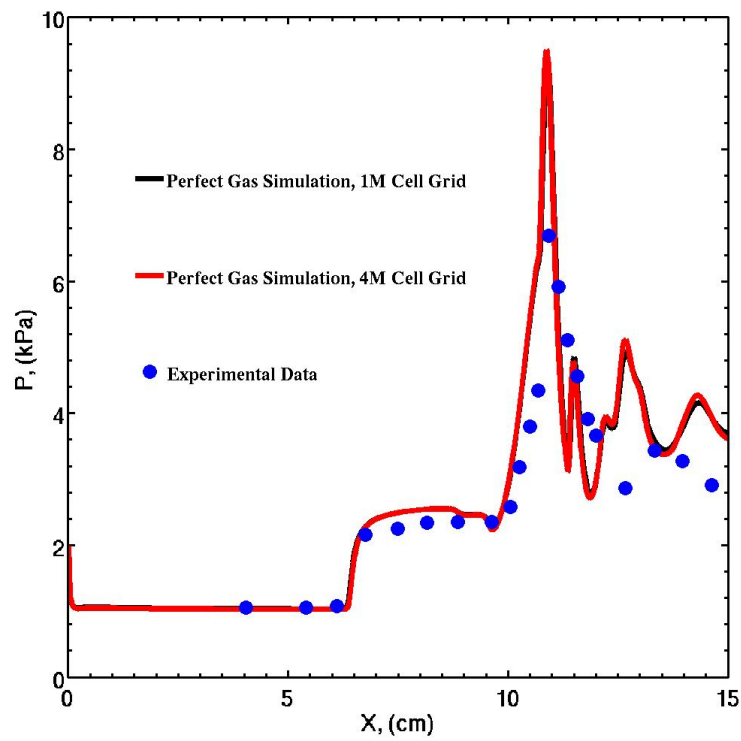
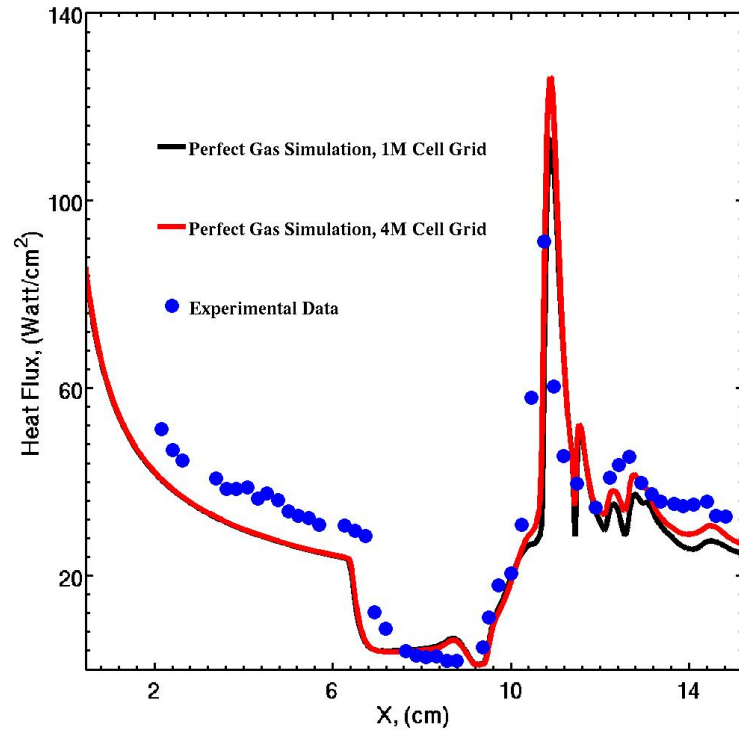


Figure 4.8: Flowfield structure for Run 4, Table 2.1



(a) Surface pressure



(b) Heat transfer rate

Figure 4.9: Computed results for Run 1, Table 2.1 for different grid refinement levels

Chapter 5

Conclusion

The objective of this study is the assessment of CFD capability for prediction of hypersonic shock wave/ boundary layer interaction at medium to high range of freestream enthalpy using the perfect gas laminar Navier-Stokes equations. The flow structure over a double cone configuration is modeled using the commercial GASPEx software for four different cases. The results are compared with the experimental data. The comparisons suggest that for the low enthalpy case, the perfect gas assumption is valid. However, for higher enthalpy cases real gas effects should be taken into account in order to accurately predict the flowfield features.

Bibliography

- [1] Gasp Version 5.1.2 Reference Guide. Aerosoft, Inc., Blacksburg, VA, 2014.
- [2] M Sharma A Dufrene and JM Austin. Design and characterization of a hypervelocity expansion tube facility. *Journal of Propulsion and Power*, 23(6):1185–1193, 2007.
- [3] R Parker T Wadhams A Dufrene, M MacLean and M Holden. Characterization of the new lens expansion tunnel facility. In *48th AIAA Aerospace Sciences Meeting*, pages 2010–1564, 2010.
- [4] JA Andreopoulos and KC Muck. Some new aspects of the shock-wave/boundary-layer interaction in compression-ramp flows. *Journal of Fluid Mechanics*, 180(1):405–428, 1987.
- [5] R Benay, B Chanetz, and J Délery. Code verification/validation with respect to experimental data banks. *Aerospace Science and Technology*, 7(4):239–262, 2003.
- [6] J Bibin, Vinayak N Kulkarni, and Ganesh Natarajan. Shock wave boundary layer interactions in hypersonic flows. *International Journal of Heat and Mass Transfer*, 70:81–90, 2014.
- [7] M Bleilebens and H Olivier. On the influence of elevated surface temperatures on hypersonic shock wave/boundary layer interaction at a heated ramp model. *Shock Waves*, 15(5):301–312, 2006.
- [8] T Bartel C Roy, M Gallis and J Payne. Navier-Stokes and direct simulation monte carlo predictions for laminar hypersonic separation. *AIAA Journal*, 41(6):1055–1063, 2003.

- [9] G Candler, I Nompelis, and M-C Druguet. Navier-stokes predictions of hypersonic double-cone and cylinder-flare flow fields. AIAA Paper 2001-1024, American Institute of Aeronautics and Astronautics, January 2001.
- [10] B Chanetz. Study of axisymmetric shock wave/boundary layer interaction in hypersonic laminar flow. Technical Report RT 42/4362 AN, Office National D'Etudes et de Recherches Aerospatiales, 1995.
- [11] B Chanetz. Low and high enthalpy shock-wave/boundary layer interactions around cylinder-flare models. In P Reijasse, D Knight, M Ivanov, and I Lipatov, editors, *EUCASS Progress in Flight Physics Volume 3*, pages 107–118. EDP Sciences and Torus Press, 2012.
- [12] B Chanetz, R Benay, J-M Bousquet, R Bur, T Pot, F Grasso, and J Moss. Experimental and numerical study of the laminar separation in hypersonic flow. *Aerospace Science and Technology*, 3:205–218, 1998.
- [13] P Canupp D Gaitonde and M Holden. Heat transfer predictions in a laminar hypersonic viscous/inviscid interaction. *Journal of Thermophysics and Heat Transfer*, 16(4):481–489, 2002.
- [14] D Drikakis D Gaitonde A Lani I Nompelis B Reimann D Knight, J Longo and L Walpot. Assessment of cfd capability for prediction of hypersonic shock interactions. *Progress in Aerospace Sciences*, 48:8–26, 2012.
- [15] J Délery and J-P Dussauge. Some physical aspects of shock wave/boundary layer interactions. *Shock Waves*, 19(6):453–468, 2009.
- [16] J Delery and AG Panaras. Shock-wave/boundary-layer interactions in high-mach-number flows. Agard Report, AGARD, 1996.
- [17] D Dolling. Fifty years of shock-wave/boundary-layer interaction research: What next? *AIAA journal*, 39(8):1517–1531, 2001.
- [18] M.-C. Druguet, G Candler, and I Nompelis. Effect of Numerics on Navier-Stokes

- Computations of Hypersonic Double-Cone Flows. *AIAA Journal*, 43(3):616–623, March 2005.
- [19] A Dufrene, M MacLean, R Parker, T Wadhams, E Mundy, and M Holden. Characterization of the new lens expansion tunnel facility. AIAA Paper 2010-1564, American Institute of Aeronautics and Astronautics, January 2010.
- [20] B Edney. Effects of shock impingement on the heat transfer around blunt bodies. *AIAA Journal*, 6(1):15–21, 1968.
- [21] M Panesi O Chazot G Degrez, A Lani and H Deconinck. Modelling of high-enthalpy, high-mach number flows. *Journal of Physics D: Applied Physics*, 42(19):194004, 2009.
- [22] K Naitou M Sun G Jagadeesh, T Hashimoto and K Takayama. Visualization of unsteady shock oscillations in the high-enthalpy flow field around double cones. *Journal of visualization*, 6(2):195–203, 2003.
- [23] J Perkins G Settles and S Bogdonoff. Investigation of three-dimensional shock/boundary-layer interactions at swept compression corners. *AIAA Journal*, 18(7):779–785, 1980.
- [24] D Gaitonde. Evaluation of flux-split schemes in laminar hypersonic flows. Oral Presentation, AIAA 39th Aerospace Sciences Meeting and Exhibit, Reno, NV, 2001.
- [25] P Gnoffo et al. CFD validation studies for hypersonic flow prediction. *AIAA paper*, 1025:2001, 2001.
- [26] N Gorchakova, L Kuznetsov, V Yarygin, B Chanetz, T Pot, R Bur, JP Taran, D Pigache, D Schulte, and J Moss. Progress in hypersonic studies using electron-beam-excited x-ray detection. *AIAA journal*, 40(4):593–598, 2002.
- [27] A Harten. High resolution schemes for hyperbolic conservation laws. *Journal of computational physics*, 49(3):357–393, 1983.

- [28] M Holden. Experimental studies of laminar separated flows induced by shock wave/boundary layer and shock/shock interaction in hypersonic flows for cfd validation. AIAA Paper 2000-0930, American Institute of Aeronautics and Astronautics, January 2000.
- [29] M Holden and J Harvey. Code validation study of laminar shock/boundary layer and shock/shock interactions in hypersonic flow, part A: Experimental measurements. AIAA Paper 2001-1031, American Institute of Aeronautics and Astronautics, January 2001.
- [30] M Holden and T Wadhams. A database of aerothermal measurements in hypersonic flow in building block experiments for cfd validation. *AIAA paper*, 1137:2003, 2003.
- [31] M Holden, T Wadhams, J Harvey, and G Candler. Comparisons between measurements in regions of laminar shock wave boundary layer interaction in hypersonic flows with navier-stokes and dsmc solutions. AIAA Paper 2002-0435, American Institute of Aeronautics and Astronautics, January 2002.
- [32] J Marvin J Delery and E Reshotko. Shock-wave boundary layer interactions. Technical Report, DTIC Document, 1986.
- [33] M Holden J Harvey and T Wadhams. Code validation study of laminar shock/boundary layer and shock/shock interactions in hypersonic flow, part B: Comparison with navier-stokes and dsmc solutions. AIAA Paper 2001-1031, American Institute of Aeronautics and Astronautics, January 2001.
- [34] B Kirk and G Carey. Validation studies of fully implicit, parallel finite element simulations of laminar hypersonic flows. *AIAA Journal*, 48(6):1025–1036, 2010.
- [35] D Knight. RTO WG 10: Test Cases for CFD Validation of Hypersonic Flight. AIAA Paper 2002-0433, American Institute of Aeronautics and Astronautics, January 2002.
- [36] D Knight. *Elements of Numerical Methods for Compressible Flows*. Cambridge University Press, 2006.

- [37] D Knight and J Longo. Shock interactions investigations associated with AVT-136. In *48th AIAA Aerospace Sciences Meeting*, 2010.
- [38] J Komives, I Nompelis, and G Candler. Numerical investigation of unsteady heat transfer on a double wedge geometry in hypervelocity flows.
- [39] R Korkegi. Survey of viscous interactions associated with high mach number flight. *AIAA Journal*, 9(5):771–784, 1971.
- [40] T Wadhams M Holden, M MacLean and A Dufrene. Measurements of Real Gas Effects on Regions of Laminar Shock Wave/Boundary Layer Interaction in Hypervelocity Flows for "Blind" Code Validation Studies. AIAA Paper 2013-2836, American Institute of Aeronautics and Astronautics, June 2013.
- [41] M Holden M MacLean and A Dufrene. Measurements of real gas effects on regions of laminar shock wave/boundary layer interaction in hypervelocity flows. AIAA Aviation, Atlanta, GA, 2014.
- [42] T Wadhams M MacLean, A Dufrene and M Holden. Numerical and experimental characterization of high enthalpy flow in an expansion tunnel facility. *AIAA Paper*, 1562:2010, 2010.
- [43] M Marini. Effects of flow and geometry parameters on shock-wave boundary-layer interaction phenomena. *AIAA paper*, pages 98–1570, 1998.
- [44] J Moss and J Olejniczak. Shock wave/boundary layer interactions in hypersonic low density flows. *AIAA Paper*, pages 98–2668, 1998.
- [45] I Nompelis, G Candler, and M Holden. Effect of vibrational nonequilibrium on hypersonic double-cone experiments. *AIAA Journal*, 41(11):2162–2169, November 2003.
- [46] I Nompelis, G Candler, M Holden, and T Wadhams. Computational investigation of hypersonic viscous/inviscid interactions in high enthalpy flows. AIAA Paper 2003-3642, American Institute of Aeronautics and Astronautics, June 2003.

- [47] B Reinartz and R Ballmann, Jand Boyce. Numerical investigation of wall temperature and entropy layer effects on double wedge shock/boundary layer interactions. In *AIAA Aerospace Sciences Meeting and Exhibit*, 2006.
- [48] Ph Roe. Approximate riemann solvers, parameter vectors, and difference schemes. *Journal of computational physics*, 43(2):357–372, 1981.
- [49] J Shinn and Ch Miller III. Experimental perfect-gas study of expansion-tube flow characteristics. *NASA STI/Recon Technical Report N*, 79:14327, 1978.
- [50] AB Swantek and Joanna Austin. Heat transfer on a double wedge geometry in hypervelocity air and nitrogen flows. In *50th AIAA Aerospace Sciences Meeting including the New Horizons Forum and Aerospace Exposition*, pages 09–12, 2012.
- [51] Robert L Trimpf. *A Preliminary Theoretical Study of the Expansion Tube: A New Device for Producing High-enthalpy Short-duration Hypersonic Gas Flows*. National Aeronautics and Space Administration, 1962.
- [52] Bram Van Leer. Flux-vector splitting for the euler equations. In *Eighth International Conference on Numerical Methods in Fluid Dynamics*, pages 507–512. Springer, 1982.
- [53] T Wadhams and M Holden. Summary of experimental studies for code validation in the lens facility and comparisons with recent navier-stokes and dsmc solutions for two- and three-dimensional separated regions in hypervelocity flows. In *42 nd AIAA Aerospace Sciences Meeting and Exhibit*, 2004.
- [54] James Withington, V Yang, and JS Shuen. A time-accurate implicit method for chemically reacting flows at all mach numbers. AIAA Paper 1991-0581, American Institute of Aeronautics and Astronautics, January 1991.
- [55] Michael J Wright, K Sinha, J Olejniczak, GV Candler, TD Magruder, and AJ Smits. Numerical and experimental investigation of double-cone shock interactions. *AIAA journal*, 38(12):2268–2276, 2000.